Experimental Mechanics (2024) 64:153–165
https://doi.org/10.1007/s11340-023-01008-y

RESEARCH PAPER

Crack Growth of Defects in Ti-6Al-4V Under Uniaxial Tension: Measurements and Modeling

E.T. Furton[1] · **A. M. Beese**[1,2]

Received: 12 June 2023 / Accepted: 5 October 2023 / Published online: 21 November 2023

Abstract

Background This study investigates the effects of pores on the mechanical properties of metals produced by additive manufacturing, which can limit strength and ductility.

Objective This research aims to both measure and model the rate of crack growth emanating from these pores in additively manufactured Ti-6Al-4 V fabricated with laser powder bed fusion.

Methods Uniaxial tensile samples containing intentionally embedded penny-shaped pores were mechanically tested to failure, and loading was interrupted by a series of unload steps to measure the stiffness degradation with load. The factors contributing to reduction in stiffness, namely (1) elastic and plastic changes to geometry, (2) the effect of plastic deformation on modulus, and (3) crack growth, were deconvoluted through finite element modeling, and the crack size was estimated at each unloading step.

Results The stiffness-based method was able to detect stable crack growth in samples with large pores (1.6% to 11% of the cross-sectional area). Crack growth as a function of strain was fit to a model where the crack driving force was based on equivalent strain and a model where the crack driving force was based on energy release rate.

Conclusions Significant crack growth occurred only after the onset of necking in samples containing small pores, while samples containing large pores experienced continuous crack growth with strain.

Keywords Crack growth · Titanium alloys · Fracture · Ductility · Finite element modeling

Introduction

In laser powder bed fusion (PBF-LB) additive manufacturing (AM), components are fabricated layer-by-layer, through the iterative spreading of powder, melting of the powder by scanning a two-dimensional pattern with a laser, and solidification of the molten metal to fuse to the layer below. PBF-LB provides design flexibility allowing for the manufacturability of complex, three-dimensional parts [1].

One challenge in adopting PBF-LB for structural applications is the variability in material properties, which can be attributed to heterogeneous microstructures, preferred crystallographic texture, and porosity [2, 3]. Pores encountered in AM are typically classified as lack-of-fusion (LOF), keyhole, bead-up, or gas entrapment [4, 5]. LOF pores have irregular, sharp morphologies that may initiate early failure due to high stress concentration factors. In this study, PBF-LB Ti-6Al-4 V was studied, the ductility of which in uniaxial tension has been shown to be sensitive to pores greater than 0.4% of the cross-sectional area [6].

Additive manufacturing provides a means for isolating the effect of individual defects on fracture behavior through the fabrication of internal pores with a specified size, shape, and location, which was not previously possible with conventional processing methods. Samples containing fabricated pores have been designed to study the effect of a single defect on fracture under various stress states [6–11].

Studies modeling crack growth have primarily investigated cracks under plane strain. In an analysis by Chobin [12], crack growth in a center-cracked-tension (CCT) 70/30 brass plate was studied. No stable crack growth was observed until the onset of necking, after which the rate of crack growth with

E.T. Furton is a member of SEM.

✉ A. M. Beese
beese@matse.psu.edu

[1] Department of Materials Science and Engineering, Pennsylvania State University, University Park, PA 16802, USA

[2] Department of Mechanical Engineering, Pennsylvania State University, University Park, PA 16802, USA

respect to engineering strain was shown to be proportional to the crack length, *a.* A differential amount of crack growth, *da*, was related to a differential change in far-field engineering strain, $d\varepsilon_{eng}$ as:

$$da = A\, a\, d\varepsilon_{eng} \tag{1}$$

where A is a proportionality constant. The primary benefit of the Chobin model is its simplicity, as engineering strain and crack size can be measured experimentally. However, the model is empirical and does not consider the microscopic processes occurring near the crack tip singularity that drive crack growth, limiting the model's potential for extrapolation.

A crack tip singularity may be characterized by the J-integral [13]. For the J-integral to uniquely describe the stress and strain fields around a crack, loading must be proportional, the material must behave elastically, and crack tip deformation cannot be excessive. Under these conditions, the J-integral is equivalent to the energy release rate, G, which is the rate of change of potential energy with respect to crack area. Although the J-integral is applicable to only a stationary crack, Rice et al. [14] used compatibility, equilibrium, and thermodynamic considerations around a plane strain crack tip to relate crack growth to the J-integral, termed the RDS model:

$$\delta_c = \frac{\alpha r_m}{\sigma_0}\frac{dJ}{da} + \beta r \frac{\sigma_0}{E} ln\left(\frac{e\lambda EJ}{r_m \sigma_0^2}\right) \tag{2}$$

where δ_c represents the crack tip opening displacement a short distance, $r_{m,}$ behind the crack tip, α, β, and λ are unitless constants, σ_0 is the yield strength, E is the Young's modulus, and e is Euler's number. The model captures the transition from stable crack growth, where the rate of crack growth with respect to strain is finite, to unstable crack growth, where the rate of crack growth is infinite.

To quantify the evolution of damage during a mechanical test, various nondestructive testing methods have been developed, including stiffness measurements, electrical resistance measurements, ultrasonic testing, and X-ray tomography [15–18]. In the compliance method, samples are periodically unloaded and the reduction in stiffness due to crack growth is measured. Bonora et al. [19] performed stiffness measurements on uniaxial mechanical tests of nearly-dense high strength steel and high purity copper, and separated geometrical effects from damage accumulation. They attributed a rapid decrease in the material's stiffness during uniform plastic deformation to damage accumulation. Yoshida et al. [20] similarly observed that the effective Young's modulus, E, decreased with the von Mises equivalent plastic strain, $\overline{\varepsilon}^p$, and proposed that the modulus, initially E_0, exponentially decayed to an asymptotic value, E_a:

$$E = E_o - (E_o - E_a)(1 - e^{-\xi\overline{\varepsilon}^p}) \tag{3}$$

where the decay constant, ξ, controls the rate at which the modulus decreases with plastic strain.

In the present study, Ti-6Al-4 V samples, containing designed internal flaws ranging from 0.37% to 11% of the gauge section's cross-sectional area, were mechanically tested, and load-unload cycles were used to measure the reduction in stiffness. Through comparison to a series of finite element models, experimental stiffness measurements were used to estimate crack growth. A Chobin-like model and a modified RDS model were calibrated to the experimental data. Both calibrated crack growth models were evaluated at a series of preexisting pore sizes, and the rates of crack growth with respect to engineering strain and the strain at which the crack became unstable, leading to fracture, were identified. This study describes a method to both measure and model crack growth from a single lack-of-fusion type pore in additively manufactured Ti-6Al-4V.

Experimental Methods

Sample Fabrication

Samples were designed in accordance with ASTM E8 [21] with the sample geometry shown in Fig. 1(a). A gauge length of 24 mm was used for all engineering strain measurements. The samples were fabricated with a ProX 320 machine (3D Systems, Rock Hill, SC), with the samples' axes colinear with the vertical build direction. After fabrication, the samples were heat treated in an argon environment at 850 °C for 2 h [22]. The samples were fabricated as cylinders and the gauge sections were machined to the final dimensions.

In each sample, a single intentional pore was designed to behave similarly to a lack-of-fusion defect; however, the pores required a finite height to prevent dross from closing the defect. Each pore was designed as a cylinder with its axis parallel to the loading direction, with a height of 240 µm (4 layers) as described in previous work [6], and located at the sample's center as shown schematically in Fig. 1(b). Due to the axisymmetric geometry and boundary conditions, crack growth for modeling was considered to be one-dimensional along the radial direction. In a previous study on Ti-6Al-4 V samples containing similar internal pores, X-ray computed tomography (XCT) identified little change in pore volume after loading to 75% of the failure strain, indicating that cracking, rather than pore growth, dominated the fracture behavior [6].

X-ray computed tomography, with a voxel size of 10 µm, was used to quantify the initial pore sizes, and the same parameters were used as in a previous study on the

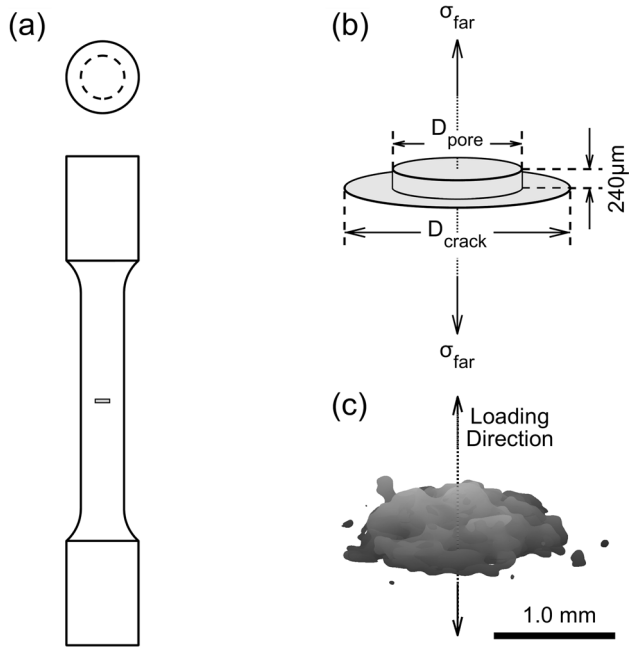

Fig. 1 (**a**) Sample dimensions, where the sample's axis was along the vertical build direction. All dimensions are in millimeters unless otherwise noted. The engineering strains were measured with 24 mm long virtual extensometers. A preexisting pore was located at the center of each sample, as shown schematically in gray. (**b**) Schematic of preexisting pore and subsequent crack growth due to far-field stress studied here. (**c**) XCT reconstruction of as-built pore with a mean diameter of 1986 μm

same material [6]. An example of a pore prior to mechanical testing is shown in Fig. 1(c). The fabricated pores were smaller than designed (Table 1), and were measured to range from 0.37% to 11% of the sample cross-sectional area. Archimedes density measurements verified that the samples were nearly fully dense, with the least dense sample having a density of 99.6%. The designed pores' volumes were too small to be detectable by Archimedes measurements. The largest pore was designed to be 0.05% of the sample's volume, while the standard error of the Archimedes measurements was 0.07%.

Table 1 Comparison of intended pore diameter to diameter measured with XCT. In all subsequent analysis, the measured pore diameters were used

Design		XCT Measurement	
Diameter (μm)	Cross-Section Fraction	Equivalent Diameter (μm)	Cross-Section Fraction
600	1.0%	365	0.37%
1200	4.0%	757	1.6%
2400	16%	1986	11%

Mechanical Testing

Mechanical testing was conducted with an electromechanical load frame (Criterion 45, MTS Systems Corporation, Eden Prairie, MN). A crosshead displacement rate of 0.007 mm/s was used for both loading and unloading, corresponding to a quasi-static strain rate of 3×10^{-4} s^{-1}. Surface deformation fields were measured with stereo-digital image correlation (DIC), where a uniform white basecoat and a black speckle pattern were applied to each sample prior to mechanical testing. Two digital cameras (GRAS-50S5M-C, Teledyne FLIR, Wilsonville, OR) recorded images at a rate of 1 Hz, and the DIC images were postprocessed by VIC-3D software (Correlated Solutions, Irmo, SC) to calculate engineering strain.

Three samples were fabricated for each of the three pore sizes (Table 1); additionally, three fully dense samples without any designed pore were fabricated. For one sample of each pore size, a monotonic test was conducted to identify the elongation to failure. For the remaining samples, the displacement to failure was divided into twenty-five equivalent steps, and after each step the sample was unloaded to 10kN, corresponding to an engineering stress of 350 MPa (e.g., Fig. 2(a) for a fully dense sample). The stiffness, k, was calculated for each load-unload cycle based on engineering stress–strain values.

Stiffness Modeling

During each mechanical test, the measured stiffness decreased because of three factors: changing sample geometry due to the elastic Poisson effect and plastic incompressibility, reduction of elastic modulus due to plastic strain, and crack growth. All three stiffness-reducing phenomena were incorporated into finite element models (Abaqus FEA, Dassault Systèmes, France).

Regarding the first factor, during uniform plastic deformation, reduction in the sample's cross-sectional area and increase in gauge length reduced the stiffness with $1/(1+\varepsilon_{eng})^2$ [19]. To capture the effect of changing geometry on the stiffness into the necking regime, the material's elasto-plastic response was defined by elastic parameters in Table 2, and an isotropic J2 plasticity model with Swift Law hardening:

$$\Delta\sigma_y = \begin{cases} nA\left(\varepsilon_o + \overline{\varepsilon}^p\right)^{n-1}\Delta\overline{\varepsilon}^p \; for \; \overline{\varepsilon}^p < 0.080 \\ K_1\Delta\overline{\varepsilon}^p \; for \; 0.080 < \overline{\varepsilon}^p \le 0.140 \\ K_2\Delta\overline{\varepsilon}^p \; for \; \overline{\varepsilon}^p > 0.140 \end{cases} \quad (4)$$

where the parameters n, A, ε_0, K_1, and K_2 were calibrated using the fully dense samples' data and are given in Table 2. As shown in Fig. 2(a), good agreement was achieved between fully-dense experimental and finite element model

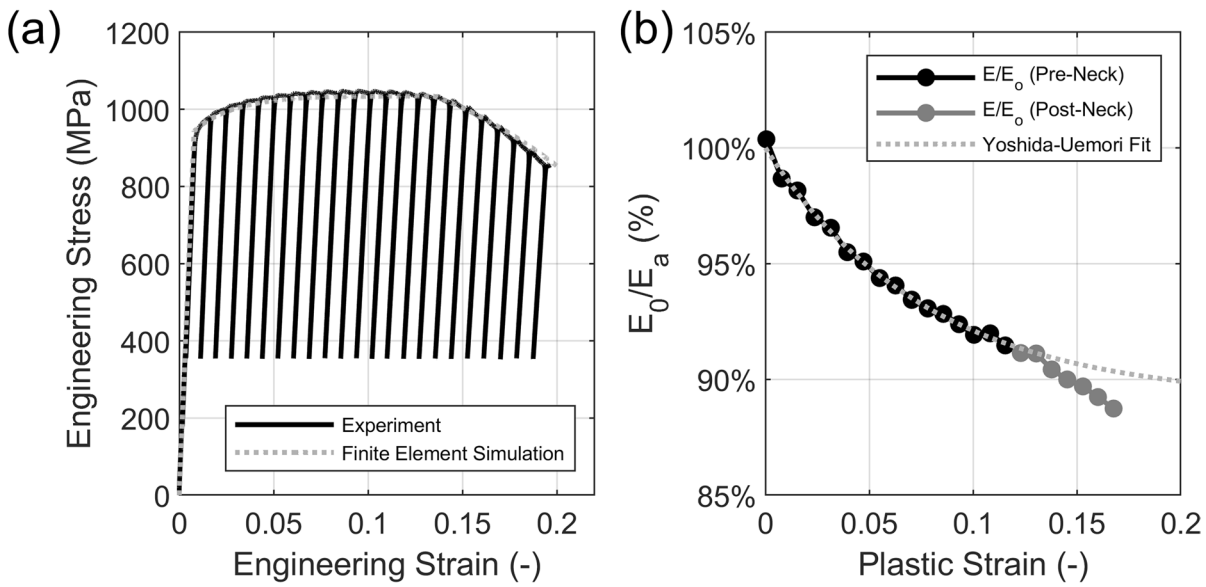

Fig. 2 (**a**) Engineering stress–strain curve of load-unload experiment and fully-dense finite element simulation on a fully dense sample. The unload steps were spaced at approximately 1/25th of the total displacement to failure and the sample was unloaded to 10 kN at each interval. (**b**) The modulus as calculated from the true-stress, true-strain curve for a fully dense sample is fit with the Yoshida-Uemori stiffness reduction model

stress–strain behavior across the elastic, uniform plastic, and necking regimes.

The degradation of modulus with plastic strain is a global effect (equation (3)) and affects material points far from the designed defect. This effect may be caused by microplasticity, point defect pinning, or an evolving texture, although it is unlikely to be the latter because the effect is most prevalent at small strains [23, 24]. The calibrated Yoshida-Uemori model is given in Fig. 2(b), and the parameters are provided in Table 2. The elastic modulus degradation was incorporated in the finite element models with a user material model (UMAT).

Any additional decrease in stiffness is attributed to a crack emanating from the designed pore, as shown schematically in Fig. 1(b). To identify the effect of cracks on stiffness, samples with circular internal cracks with diameters ranging from 300 µm to 4200 µm (0.25% to 49% cross-sectional area) were modeled. The cracks were modeled as having zero height and traction-free surfaces. Elements near the crack tips had edge lengths of 20 µm. In each individual model, the crack tip was stationary, as these simulations were used to measure stiffness.

Finite element simulations were loaded and unloaded at increments of 0.5% engineering strain to calculate the stiffness. The relationship between stiffness, initial crack diameter, and engineering strain is given in Fig. 3(a). The stiffness decreases with engineering strain in all cases, with the reduction due to crack size a secondary effect.

The rate of change in stiffness with respect to engineering strain is shown in Fig. 3(b). There is little decrease in stiffness in the elastic regime regardless of pore size. After yielding the stiffness decreases sharply due to degradation of stiffness with plastic strain, the thinning cross-section, and elongating gauge length.

The sensitivity of the compliance method for determining crack size is inversely proportional to the rate of change of the stiffness with respect to crack size, $\frac{\partial k}{\partial a}$, which is shown in Fig. 3(c). The uncertainty of crack radius, δ_a, due to an uncertainty in the stiffness, δ_k, is:

$$\delta_a = \left(\frac{\partial k}{\partial a}\right)^{-1} \delta_k \tag{5}$$

The uncertainty of stiffness is dictated by the repeatability of the method used to measure displacement (here DIC). When accounting for sample geometry effects and modulus

Table 2 Calibrated material parameters for elastic behavior, strain hardening, and modulus degradation

Elastic Properties		Swift Law					Yoshida-Uemori Parameters	
E_o (GPa)	Poisson's ratio (-)	n (-)	A (MPa)	ε_o (-)	K_1 (MPa)	K_2 (MPa)	E_a (GPa)	ξ (-)
120.9	0.30	0.090	1389	0.014	1195	400	107.7	12.8

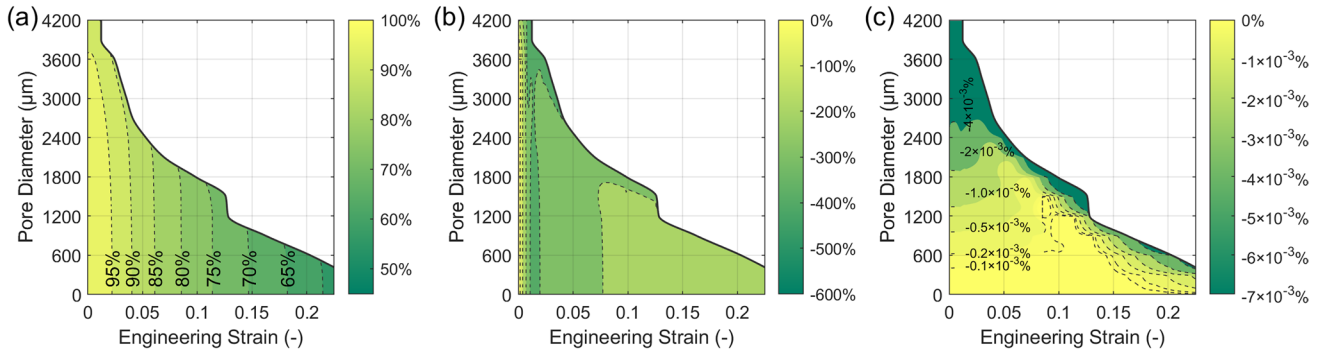

Fig. 3 Contour plots of (**a**) relative stiffness, k/k_0, where k_0 is the stiffness of a sample without a crack and at zero strain, as a function of reference configuration penny-shaped crack's diameter and engineering strain, where 100% signifies no reduction; (**b**) partial derivative of the stiffness with respect to engineering strain, with units expressed in terms of percent change per unit engineering strain; and (**c**) partial derivative of the stiffness with respect to pore radius, with units of percent change per micron

degradation due to plastic strain, the stiffness measurements were found to be approximately normally distributed with a standard deviation of 0.26%. The contours of Fig. 3(c) correspond to uncertainties tabulated in Table 3. At moderate strains (< 14%) and small initial pore sizes (850 μm diameter, or < 2% cross-sectional area), the compliance method is not sensitive to crack growth. This limitation is less severe for smaller pores beyond the onset of necking, or for larger pores with a diameter greater than 1500 μm (6.3% of the cross-sectional area), where crack growth on the order of 100's of microns may be resolved over the uncertainty of stiffness measurements.

The crack size at a given engineering strain for a measured stiffness was estimated using the data in Fig. 3(a). Because of the uncertainty in the stiffness measurement, it was treated as a random, normally distributed variable with a mean of the experimentally measured value and with a standard deviation of 0.26%, as discussed above. The calculation of crack size is schematically shown in Fig. 4, where the relationship between crack size and stiffness obtained from finite element modeling is used to transform the distribution of stiffness to crack size estimates. The transformation is non-linear; a normal distribution of stiffness is transformed to a non-normal, negatively skewed distribution of crack size. For a small confidence interval (e.g., 1%), the estimate of crack size falls within a narrow bound, but there is a large probability for Type II error where the true crack size falls outside of the confidence bound; conversely, a large confidence interval (e.g., 99%) decreases the probability of Type II error, but at the expense of increasing the range of considered crack sizes [25].

Table 3 Uncertainty in crack diameter due to a 0.26% uncertainty in the stiffness

Sensitivity (%/μm)	Crack Diameter Uncertainty (μm)
-0.1×10^{-3}	2600
-0.2×10^{-3}	1300
-0.5×10^{-3}	520
-1.0×10^{-3}	260
-2.0×10^{-3}	130
-4.0×10^{-3}	65

Crack Growth Models

Both the Chobin-like and modified RDS models were reformulated so that an increment of crack growth, da, was expressed in terms of an increment of far-field engineering strain, $d\varepsilon_{eng}$ [12, 14].

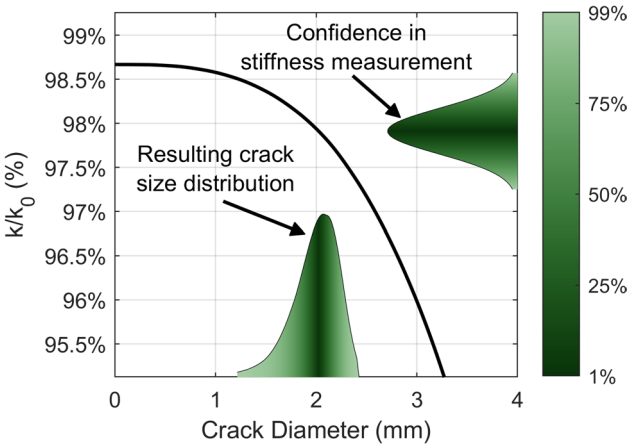

Fig. 4 Transformation of relative stiffness distribution (shown on y-axis) to crack size distribution (shown on x-axis), shown for a sample containing a 2 mm pore (11% cross-sectional area) at an engineering strain of 0.8%. The distribution of the stiffness measurement, with confidence intervals indicated by color, is assumed to be normally distributed. The crack diameter is related to the stiffness through finite element modeling, given as the solid black curve

Chobin-like model

Chobin reported that stable crack growth during monotonic loading was only observed after the onset of necking, and therefore equation (1) is only applicable in that regime [12]. In this study, to generalize the equation so it is applicable to the elastic, uniform plastic, and localized plastic regimes, the rate of crack growth with respect to engineering strain was assumed to be a separable function of equivalent strain and crack size. If a is zero, da must necessarily be zero, while da can be nonzero for a differential amount of strain. A function that satisfies the above requirements is:

$$da_{plane\ strain} = A(e^{a/n} - 1)\left(e^{\varepsilon_{tot}/m} - p\right)d\varepsilon_{eng} \tag{6}$$

where A, n, m, and p are calibration coefficients. A is the proportionality constant from Chobin's previous analysis. The term $(e^{a/n} - 1)$ depends only on crack-size; if there is no initial crack, this term is zero and precludes crack growth. The coefficient n controls the nonlinearity of crack growth; if n is large, the crack driving force is approximately linearly proportional to crack size, whereas a small value of n implies the crack driving force exponentially increases with crack size.

The final term, $\left(e^{\varepsilon_{tot}/m} - p\right)$, depends only on strain, where m behaves similarly to n. At zero strain, p controls this term's magnitude. For $p=1$, there is no differential crack growth in the unloaded state even with a differential increment of strain, while a decreasing value of p increases the initial crack driving force. A measure of total strain, ε_{tot}, is calculated in a fully dense finite element simulation at the location corresponding to the crack tip, and is given as:

$$\varepsilon_{tot} = \frac{\overline{\sigma}_{VM}}{E} + \overline{\varepsilon}^{p}_{VM} \tag{7}$$

As the crack grows, the measure of total strain is considered at the new location. However, the spatial gradient of strain is small, as shown in Fig. 5(a).

For a crack under plane strain for which the Chobin model was initially derived, the crack's area grows linearly with crack length. However, for axisymmetric crack growth, the crack's area grows quadratically with crack length. The increments in crack area of cracks under plane strain (width, W, and crack length, $a_{plane\ strain}$) and axisymmetric cracks (radius, $a_{axisymmetric}$) are given as:

$$\begin{aligned} dA_{plane\ strain} &= W da_{plane\ strain} \\ dA_{axisymmetric} &= 2\pi a_{axisymmetric} da_{axisymmetric} \end{aligned} \tag{8}$$

Here, to relate the two crack types, it is assumed that the axisymmetric crack's initial radius and the initial length of the crack under plane strain are equal, given as a_0, and that both cracks initially have equivalent cross-sectional area ($W a_0 = \pi a_0^2$). The increments of crack area are set equal to one another to give:

$$da_{plane\ strain} = \frac{2a_{axisymmetric}}{a_0} da_{axisymmetric} \tag{9}$$

Substituting equation (9) into equation (6),

$$da_{axisymmetric} = A(e^{a/n} - 1)\left(e^{\varepsilon_{tot}/m} - p\right)\left(\frac{a_0}{2a}\right)d\varepsilon_{eng} \tag{10}$$

Compared to the equation for crack growth under plane strain conditions, the additional term $(\frac{a_0}{2a})$ corresponds to the added resistance to crack growth due to an increase in crack perimeter, and thus fracture process zone volume.

The Chobin-like model assumes that the crack driving force depends only on crack size and equivalent strain. However, it has been shown that ductile fracture depends not only on equivalent strain but also on stress state (e.g.,

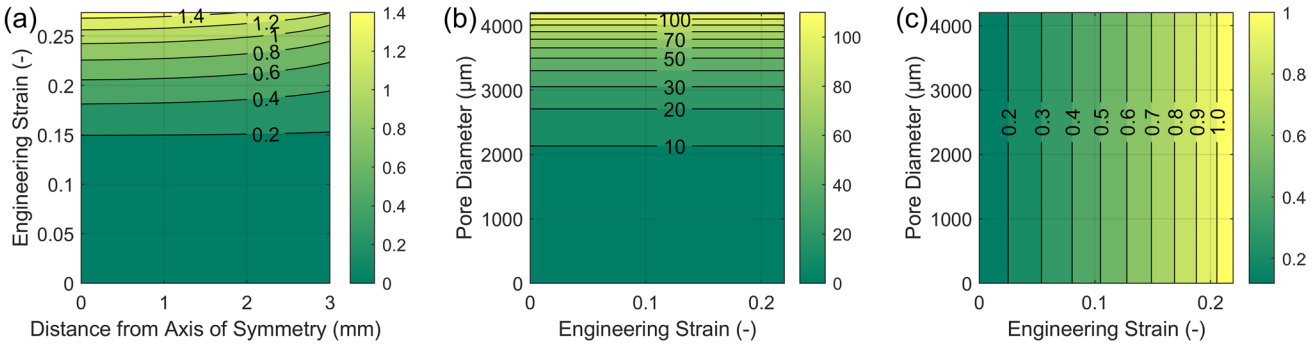

Fig. 5 (**a**) Color contours of measure of total strain in a fully dense sample as a function of engineering strain and distance from the axis of symmetry, used in the Chobin-like crack growth model. Beyond the onset of necking, the measure of total strain increases faster than the engineering strain, and is smallest near the sample's surface. The crack driving force contribution for the Chobin-like model, equation (10), is a product of the (**b**) crack-size term, $(e^{a/n} - 1)$, and (**c**) strain-based term, $\left(e^{\varepsilon_{tot}/m} - p\right)$, evaluated for parameters in Table 4. The crack-size term exhibits exponential behavior, whereas the strain-based term is approximately linear in the range of pore sizes and engineering strains studied

stress triaxiality and normalized Lode angle parameter [26, 27]). Because this study only considered uniaxial tension where the stress state was similar for all samples, stress state-dependent fitting parameters were not incorporated in equation (10).

Modified RDS model

In the derivation of the RDS model, Rice et al. stated that when only a single crack front is present, the crack tip singularity's J-integral is only a function of crack size and must be equal to the applied J-integral, J_A, which is a function of both crack size and another value that monotonically increases with the intensity of loading [14]. In this study, the monotonically increasing parameter was taken to be the far-field engineering strain. Equating J with J_A, and taking the total derivative:

$$\frac{dJ}{da} = \frac{\partial J_A}{\partial a} + \frac{\partial J_A}{\partial \varepsilon_{eng}} \frac{d\varepsilon_{eng}}{da} \tag{11}$$

Substituting equation (11) into equation (2), the increment of crack growth is written as:

$$da_{plane\ strain} = \frac{{}^{\partial J_A}/_{\partial \varepsilon_{eng}}}{\frac{\delta_c}{r_m}\frac{\sigma_o}{\alpha} - \frac{\beta(\sigma_o)^2}{E\alpha}\ln\left(\frac{e\lambda E J_A}{r_m(\sigma_o)^2}\right) - \frac{\partial J_A}{\partial a}} d\varepsilon_{eng} \tag{12}$$

and the calibrated values for α, β, λ/r_m, and δ_c/r_m are given in Table 4.

The first term in the denominator, $\frac{\delta_c}{r_m}\frac{\sigma_o}{\alpha}$, is the material's intrinsic resistance to crack growth, and the second term, $\frac{\beta(\sigma_o)^2}{E\alpha}\ln\left(\frac{e\lambda E J_A}{r_m(\sigma_o)^2}\right)$, is due to a moving stress singularity. The final term, $\frac{\partial J_A}{\partial a}$, accounts for instability; as this term's magnitude increases, the rate of crack growth accelerates. During necking, this term dominates the other terms, causing the rate of crack growth to become infinite.

As with the Chobin-like model, the RDS equation was derived for the growth of cracks under plane strain and must be modified to account for increasing crack perimeter. It was found that the factor derived in equation (9) underpredicted the ductility of samples containing small cracks, so to better capture experimental data, the $\left(\frac{2a}{a_0}\right)$ term was cubed. Additionally, for the large deformations in this study, the J-integral does not uniquely characterize the crack-tip singularity, but rather the energy release rate, G, was used to quantify its severity:

$$da_{axisymmetric} = \frac{{}^{\partial G}/_{\partial \varepsilon_{eng}}}{\left(\frac{2a}{a_0}\right)^3\left(\frac{\delta_c}{r_m}\frac{\sigma_o}{\alpha} - \frac{\beta(\sigma_o)^2}{E\alpha}\ln\left(\frac{e\lambda EG}{r_m(\sigma_o)^2}\right)\right) - \frac{\partial G}{\partial a}} d\varepsilon_{eng} \tag{13}$$

It has been shown that stress fields around axisymmetric cracks are more diffuse than cracks under plane strain [28]. Therefore, the authors hypothesize that cubing the magnitude of the factor derived in equation (9) offsets the overestimation of the axisymmetric crack's severity.

To calculate the energy release rate for a given crack size, two finite element models were used: one with a crack diameter 5 μm larger, and the other with a crack diameter 5 μm smaller, than the nominal crack size. The energy release rate describes the rate of change of strain energy, dU, with respect crack area, dA, and was approximated with the difference quotient:

$$G(\varepsilon_{eng}) = -\left.\frac{dU}{dA}\right|_{\varepsilon_{eng}} \approx -\left.\frac{\Delta U}{\Delta A}\right|_{\varepsilon_{eng}} \tag{14}$$

As with the stiffness simulations, axisymmetric finite element simulations were performed on samples containing stationary cracks with diameters up to 4200 μm (49% of cross-sectional area). Cubic spline interpolation was performed to obtain the energy release rate as a continuous function of engineering strain and crack diameter, as shown in Fig. 6(a).

The partial derivative of G with respect to engineering strain, as shown in Fig. 6(b), is small for small cracks (< 850 μm, or 2% cross-sectional area) at moderate strains (< 14% cross-sectional area). The crack driving force in this regime is small, corresponding to limited crack growth. Because strain localizes in the neck, the rate of increase of G with respect to far-field engineering strain accelerates after the onset of necking. The partial derivative of G with respect to crack size, as shown in Fig. 6(c), affects the stability of crack growth (equation (13)). At small strains, regardless of crack size, this term is small. In the necking regime, this value rapidly increases and leads to sudden crack growth and subsequent fracture. For large cracks, this term is small but G is large; the crack growth rate is therefore non-zero but the rate does not change significantly with increased far-field strain.

The authors emphasize that the energy release rate was used in this study to approximate the severity of a defect of a given size, area-fraction, and stress–strain history, and is not necessarily consistent with the measurement of J-integrals with standard fracture toughness tests. Rather than precracking the pores as with fracture toughness samples, the pores instead were intended to behave as those inside in-service components; it is likely that some blunting occurred prior to crack initiation. Additionally, during full-ligament yielding, J no longer uniquely defines the crack tip and the assumptions used in the derivation of the RDS model are not satisfied; however, G is still related to the severity of the crack. Finally, the crack tip constraint for an axisymmetric, penny-shaped crack in uniaxial tension is less severe than in typical fracture toughness specimens [29].

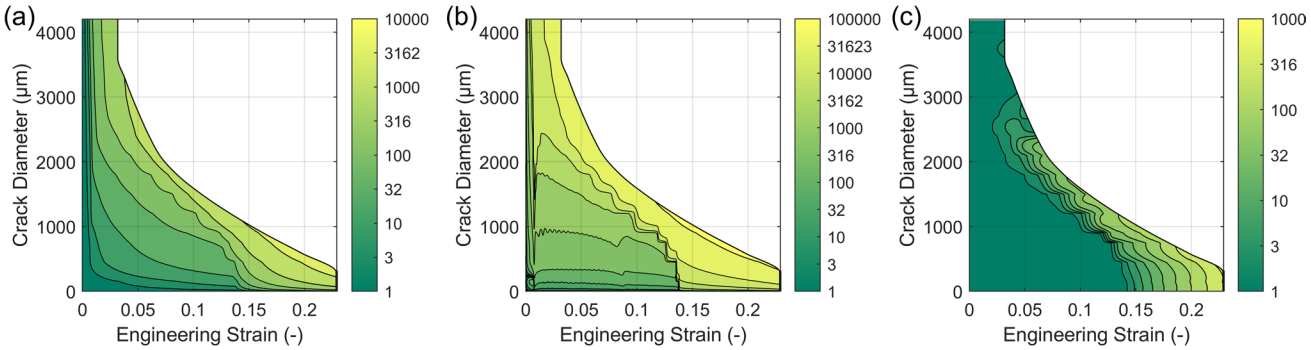

Fig. 6 Contour plots of (**a**) energy release rate, in kJ/mm^2, as a function of crack diameter and engineering strain; (**b**) the partial derivative of the energy release rate with respect to engineering strain, in kJ/mm^2 per unit strain; and (**c**) the partial derivative of the energy release rate with respect to the crack radius in kJ/mm^2 per micron. The contours are spaced at exponentially increasing intervals

Results and Discussion

Mechanical Testing

The stiffnesses, measured during unloading and subsequent reloading, as a function of engineering strain are shown in Fig. 7. The reduction of stiffness was consistent for each size of designed pore whether it was measured during unloading or reloading. For the fully dense samples, shown in Fig. 7(a), a dashed line shows the decrease in stiffness due to cross-sectional area reduction for uniform plastic deformation. It is assumed that there is negligible crack growth in the fully dense sample, and therefore the large disparity between the experimentally measured stiffness and the changing geometry is ascribed to the degradation of Young's modulus with plastic strain, as described by the Yoshida-Uemori equation.

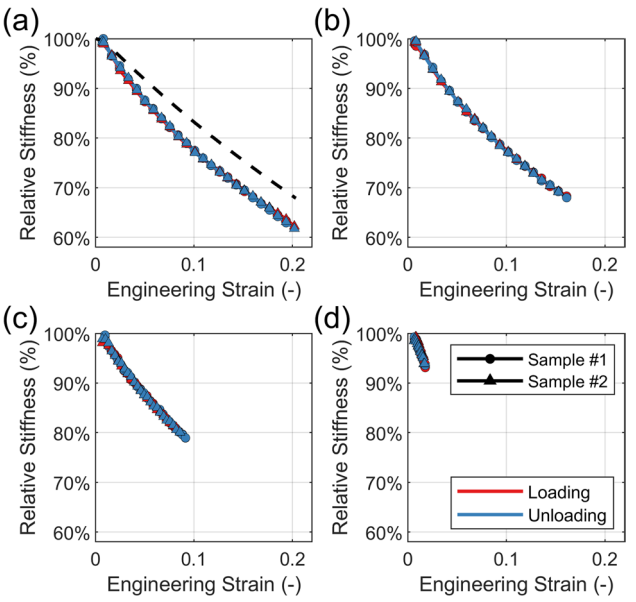

Fig. 7 Stiffness measurements for (**a**) two fully dense samples, and two samples containing a pore with initial diameter of (**b**) 365 μm (0.37% cross-sectional area), (**c**) 757 μm (1.6% cross-sectional area), and (**d**) 1986 μm (11% cross-sectional area) within 6 mm diameter gauge cross-sections. The stiffness is shown for two samples, calculated for both the unloading and reloading curves. For the fully dense samples in (**a**), the calculated stiffness decreases faster than that due to reduction in cross-sectional area alone due to the Poisson effect and plastic incompressibility (shown with the dashed line)

Each stiffness measurement was converted to a series of crack size confidence intervals with the method illustrated in Fig. 4. The final crack size measurement and confidence intervals were based on fracture surface micrographs, as described and shown in Fig. S1 of the supplementary information. For small pores, namely the sample containing a 365 μm pore (0.37% of the cross-sectional area) as shown in Fig. 8(a), at small strains the compliance method had low sensitivity and the confidence bounds are initially large (e.g., the 99% confidence bound of crack diameter ranges from 0 to 2 mm) and do not provide useful information on crack size. However, with increasing strains the compliance method's sensitivity increases, the confidence intervals narrow, and the upper bound of crack size decreases with increasing strain. As cracks do not decrease in size, this upper bound is applicable to measurements made at smaller strains. For the sample containing a pore with a diameter of 365 μm, for the final stiffness measurement at an engineering strain of 15.3%, the compliance measurement provided only 54% confidence that the crack was larger than the initial diameter, and the upper bound for the 99% confidence interval was a crack with a 1075 μm diameter. Fracture occurred shortly afterwards, at an engineering strain of 16.0%, where the fracture surface micrographs suggested the crack rapidly grew to its final size of approximately 3500 μm before final failure.

For larger pores – especially the 1986 μm pore (11% of cross-sectional area) as shown in Fig. 8(c) – the compliance method is more sensitive. Confidence intervals of crack growth conclusively show a crack steadily growing with engineering strain.

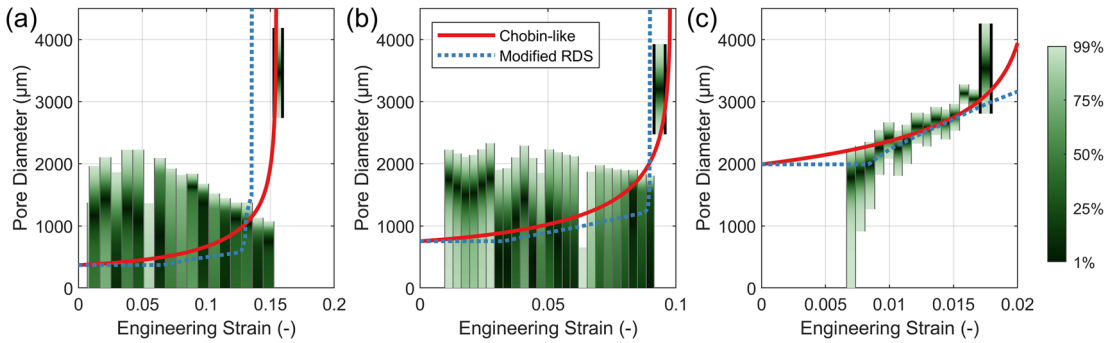

Fig. 8 Crack growth confidence bounds, for pores with initial size of (**a**) 365 μm (0.37% cross-sectional area), (**b**) 757 μm (1.6% cross-sectional area), and (**c**) 1986 μm (11% cross-sectional area). The final confidence intervals, which are bracketed in thicker vertical lines, are fracture surface measurements, whereas the other confidence intervals are derived from stiffness measurements. The fitted Chobin-like and modified RDS models for crack growth are superimposed

Parameter Fitting

Given an initial crack size, the Chobin-like and modified RDS models were numerically integrated to obtain the crack size as a function of applied macroscopic engineering strain. An optimization code (fmincon, MATLAB 2022b, MathWorks, Natick, MA) identified best fit parameters. The final crack size measurement from the fracture surface micrograph had the same weight as the contribution from all compliance-based measurements. The best-fit parameters for each model are given in Table 4 and the crack growth curves, as a function of engineering strain, are superimposed on the crack size measurements in Fig. 8.

A parametric study was performed on the two crack growth models. The displacement to failure was defined as when the crack size reached half the sample's cross-sectional area, and the initial pore diameter was varied from fully dense to 4 mm. For the Chobin-like model, the parameter A inversely correlates to failure strain for all pore sizes, as shown in Fig. 9(a). The parameter n, shown in Fig. 9(b), controls the failure strain of large cracks, while the parameter m, shown in Fig. 9(c), has the greatest impact on the strain to failure for small cracks. The parameter p, as shown in Fig. 9(d) most affects the failure strain of medium-sized cracks, ranging from 500 μm to 1000 μm (0.7%-2.8% cross-sectional area).

Although only the displacement to failure is shown in Fig. 9, the models were fit using both the intermediate crack sizes using compliance measurements and the final crack size using fracture surfaces. Based on strain to failure considerations alone, the parameters are non-unique, because an increase in both m and n could be offset by a decrease in A. The non-uniqueness, coupled with the model not incorporating the physics of crack growth, limit the model's potential for extrapolation where preexisting defects are outside of a range of 365 μm and 1986 μm (0.37% to 11% cross-sectional area).

In the modified RDS model, the parameters α, shown in Fig. 10(a), and δ_c/r_m, shown in Fig. 10(d), were inversely related, where increasing α reduced the strain to failure across a wide range of pore diameters, while increasing δ_c/r_m resulted in the opposite behavior. The parameter β (Fig. 10(b)) had an asymmetric effect, where decreasing β had little effect on the strain to failure whereas an increased β decreased the strain to failure. Finally, the parameter λ/r_m had negligible effect on the strain to failure (Fig. 10(c)) such that the modified RDS model, in the context of this study, reduces to a three-parameter model.

Crack Growth Models

Chobin-like model

In the Chobin-like model, the crack growth rate is a separable function of crack size and strain as described in equation (10), and the magnitude of each component is shown in Fig. 5(b)–(c). For the crack-size based term, $(e^{a/n}-1)$, the scaling parameter, n, is 0.33 mm and small compared to the sizes of cracks in this study; therefore, the crack driving force rises exponentially with crack size, as shown in

Table 4 Calibrated parameters for Chobin-like and modified RDS models

Chobin-Like Model				Modified RDS Model			
A (mm)	n (mm)	m (-)	p (-)	α (-)	β (-)	δ/r_m (-)	λ/r_m (m^{-1})
5.29	0.33	0.44	0.88	9.06	0.68	0.262	4.3×10^5

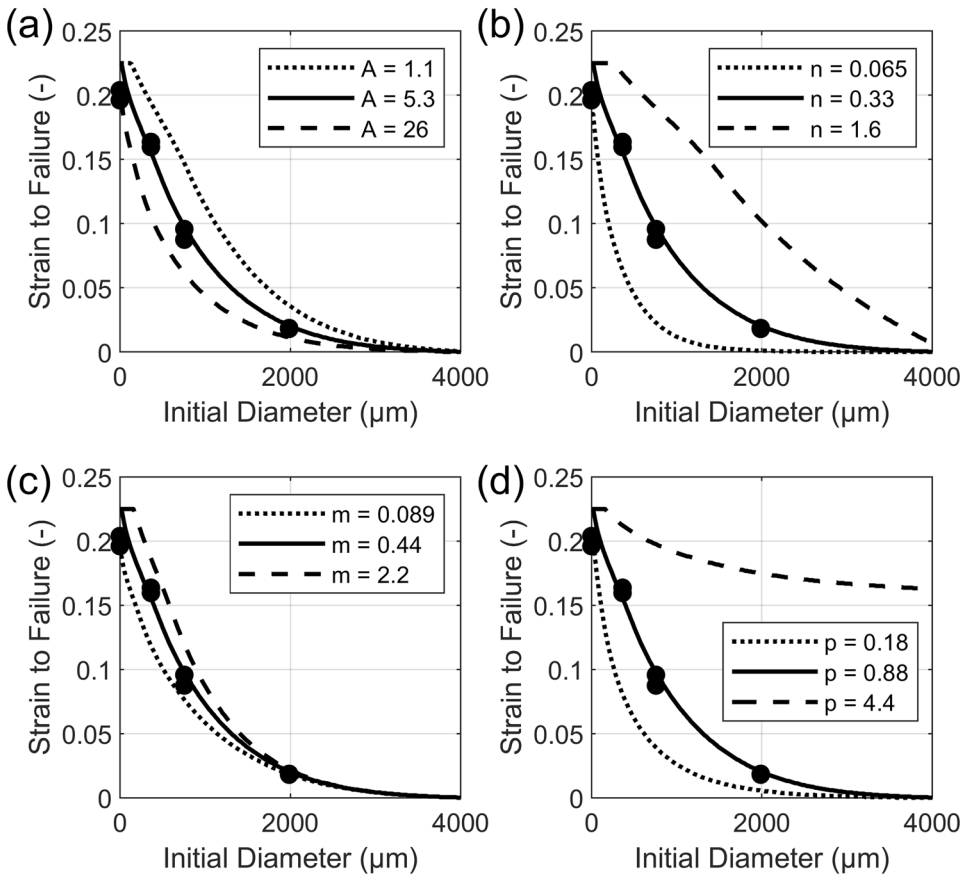

Fig. 9 Parameter study for the Chobin-like model investigating the effects of: (**a**) A, (**b**) n, (**c**) m, and (**d**) p on the strain to failure versus initial pore diameter. In each case, the parameter of interest was perturbed by a factor of $^1/_5$ and 5, while the other parameters were held constant at their values in Table 4. The displacement to failure was calculated with the preexisting pore size ranging from 0 to 4000 μm. The black dots are experimentally determined strains at fracture for the given preexisting pore diameters

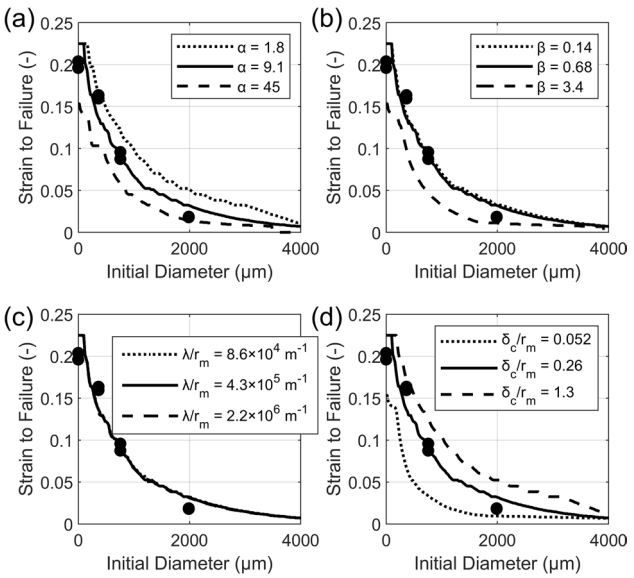

Fig. 10 Parameter study for the modified RDS model investigating the effects of: (**a**) α, (**b**) β, (**c**) λ/r_m, and (**d**) δ_c/r_m on the strain to failure versus preexisting pore diameter. In each case, the parameter of interest was perturbed by a factor of $^1/_5$ and 5, while the other parameters were held constant at their values in Table 4. The displacement to failure was calculated with the preexisting pore size ranging from 0 to 4000 μm. The black dots represent experimentally determined strains at fracture for the given preexisting pore diameters

Fig. 5(b). In this model, the growth of large cracks increases the crack driving force, which in turn causes the crack to grow larger; this positive feedback loop results in runaway crack growth. The strain-based term, $\left(e^{\varepsilon_{tot}/m} - p\right)$, shown in Fig. 5(c), behaves more linearly, only gradually increasing through the range of engineering strains in this study. The Chobin-like model indicates that crack growth is more sensitive to current crack size than applied strain.

The Chobin-like model predicts a gradual and consistent increase in crack diameter with increasing strain, as shown in Fig. 8, unlike the modified RDS model. Even for small cracks, the Chobin-like model suggests that crack growth is non negligible; this feature is not consistent with the results of the compliance-based stiffness measurements where the Chobin-like model's crack growth falls outside the 99% confidence intervals for the 365 μm diameter (0.37% cross-sectional area) pore at strains near fracture in Fig. 8(a).

Modified RDS model

For small preexisting pores at small displacements, the RDS model suggests negligible crack growth. Only after the onset of necking is crack growth non-negligible, but

due to the rapid increase in G with respect to engineering strain in the necking regime, there is only brief stable crack growth prior to fracture. For large cracks, even prior to necking, G is large and the instability factor is small, and therefore the crack grows in a stable manner.

If the material's intrinsic resistance to crack growth, δ_c / r_m, would be increased, as shown in Fig. 10(d), the strain to failure would greatly increase for samples containing large pores. However, for samples containing small pores, the instability factor dominates crack growth in the necking regime, and there would be negligible increase in the strain to failure. To increase ductility, rather than increasing a sample's crack growth resistance, the onset of necking would need to be delayed.

Model comparison

To compare the two models, both crack growth models were extrapolated, with initial pore diameters ranging from fully dense to 4000 μm (44% of the cross-sectional area) and the strain to failure (taken as when the crack grew to half the sample's cross-sectional area) is shown in Fig. 11(a). Both crack growth models agree well with experimentally measured failure strains.

In the crack-containing finite element models, the crack tip was modeled as stationary, and therefore the onset of necking and subsequent loss in load-carrying capacity was exclusively due to plasticity effects. Three distinct regions were identified: the elastic, uniform plastic, and necking regimes. The 0.2% offset rule was used to calculate the transition between the elastic and uniform plastic regions, and the criterion from ASTM E8 7.9.3.2 was used to delineate the uniform plastic from the necking regime [21]. Because the stationary crack tip finite element models did not have a fracture criterion, failure was assumed to occur when the sample lost 28% of its peak load carrying capacity, as observed experimentally with fully dense samples; as the force rapidly decreased over a small interval of engineering strain, the specific value of 28% has little effect on the defined failure strain.

The elastic, uniform plastic, and necking regimes from the stationary crack-tip finite element models are superimposed on the crack growth models' displacements to failure in Fig. 11(a). Although the stationary finite element models identify that increasing initial pore size expedites the onset of necking and loss in load-carrying capability, they greatly underestimate the effect of crack size on the failure strain. This discrepancy shows that the reduction of stiffness due to the presence of the crack alone

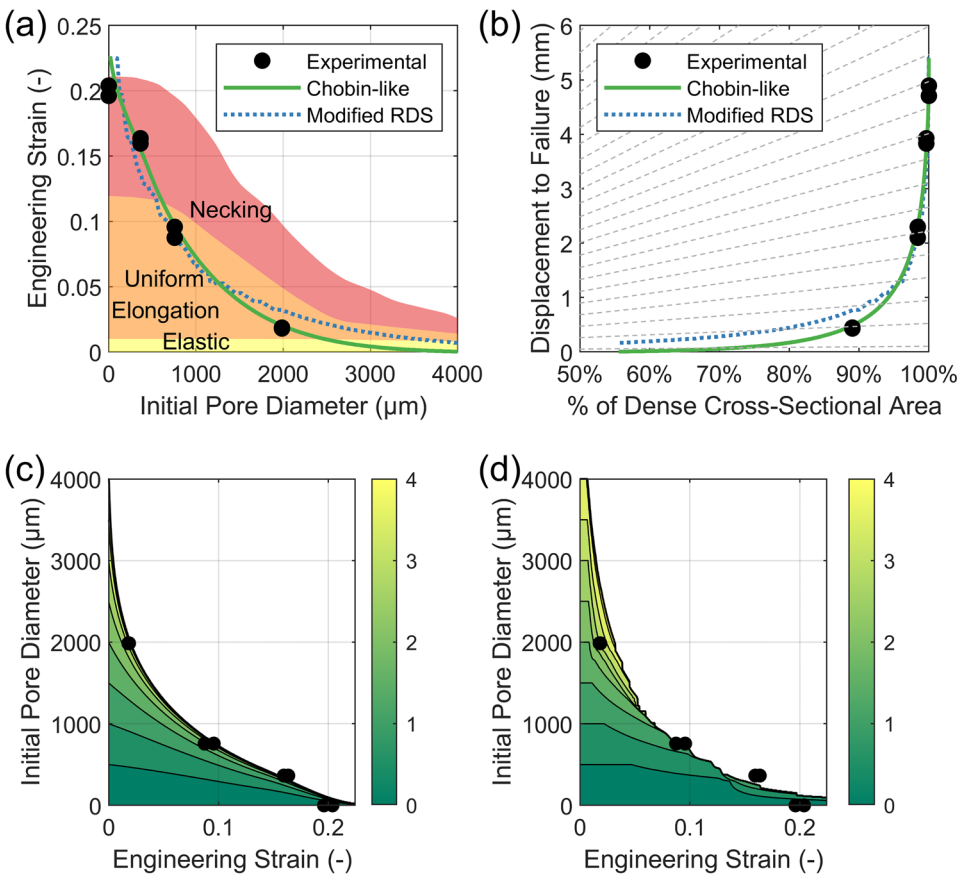

Fig. 11 (**a**) Extrapolated displacement to failure for the Chobin-like and modified RDS crack growth models as function of preexisting pore diameter. Regions of elastic, uniform plastic, and necking deformation from finite element simulations with a stationary crack are shaded. (**b**) Extrapolated displacement to failure from the crack growth models are compared against the fraction of remaining cross-sectional area. The dashed lines emanate from origin, and ductility is directly proportional to remaining cross-sectional area along these lines. Contours of the crack diameter, in millimeters, as a function of engineering strain and preexisting pore diameter, for the (**c**) Chobin-like and (**d**) modified RDS models

is insufficient for modeling the ductility in PBF-LB Ti-6Al-4 V uniaxial tension samples. When crack growth is accounted for with either the Chobin-like or RDS model, the growing crack size leads to necking at smaller strains, and this localization accelerates the rate of crack growth. The discrepancy between models with and without a moving crack tip is negligible for pores smaller than 100 μm (0.03% cross-sectional area), because even without crack growth, the sample would lose its load carrying capability due to plasticity effects alone. Conversely, for larger pores, the discrepancy becomes more pronounced, e.g., for a 1000 μm pore, or 3% of the cross-sectional area, finite element modeling with a stationary crack tip suggests loss in load-bearing capacity at an engineering strain of 18%, whereas both the Chobin-like and RDS crack growth models suggest fracture would occur at a substantially lower engineering strain of 7%.

If the Chobin-like model is extrapolated to crack sizes greater than 1986 μm (11% of the cross-sectional area), samples are predicted to fracture early in the elastic regime, whereas the RDS model predicts that large flaws will result in fracture near the yield point. Both models predict a wide range of strains to failure for cracks smaller than 365 μm (0.4% of the cross-sectional area). The upper bound for stochastic pores in PBF-LB ranges between 60 μm to 220 μm [30], and extreme value statistics may be the cause of large variances in the strain to failure between otherwise identical nearly-dense samples.

The models' displacements to failure as a function of percentage of cross-sectional area relative to a dense sample are shown in Fig. 11(b), where the dashed lines emanating from origin indicate ductility being proportional to cross-sectional area loss. For small cracks (smaller than 10% of cross-sectional area loss), the effect of crack size on ductility is more significant than loss of cross-sectional area alone would suggest. For cracks larger than 10% of the cross-sectional area, the models suggest that the ductility is approximately proportional to area-loss fraction.

The crack diameter as a function of initial pore size and engineering strain is compared for the Chobin-like model in Fig. 11(c) and the modified RDS model in Fig. 11(d). For the Chobin-like model, even at small displacements non-negligible crack growth is predicted. Conversely, the modified RDS model in Fig. 11(d) predicts an incubation period of negligible crack growth. For samples with small pores, crack growth is minimal until necking, while large cracks continually grow after the sample yields.

Conclusions

In this study, PBF-LB Ti-6Al-4 V uniaxial tension samples containing internal preexisting flaws were tested to fracture with cyclic load/unload cycles to measure the stiffness and nondestructively evaluate crack growth. Finite element analyses were used to decouple the effect of stable crack growth from other factors that reduce stiffness during elasto-plastic loading, and used to calibrate two crack growth models. This study's primary conclusions are:

- For small preexisting pores (< 2% cross-sectional area), the change in stiffness during an unloading cycle was found to be insensitive to crack growth at moderate displacements (< 14% engineering strain). However, in this regime, the crack driving force was also small.
- For large preexisting pores (11% of the cross-sectional area), the stiffness-based crack-size measurement method conclusively identified stable crack growth after the sample yielded.
- A Chobin-like crack growth model identified that the crack driving force grew exponentially with crack size, but only approximately linearly with strain.
- According to the RDS crack growth model, small pores (< 2% cross-sectional area) experienced minimal crack growth prior to sudden, unstable growth in the necking regime, while large cracks steadily grew at small displacements. The instability factor was geometry dependent, and the onset of unstable crack growth may behave differently for different sample geometries.
- Under uniaxial tension, both the Chobin-like and RDS crack growth models suggest that for cracks larger than 10% of the cross-sectional area, the ductility is approximately proportional to area-loss fraction. However, as crack size decreases below 10% of the cross-sectional area, the ductility sharply exceeds that proportional to area-loss fraction.

Supplementary Information The online version contains supplementary material available at https://doi.org/10.1007/s11340-023-01008-y.

Acknowledgements The financial support provided by the National Science Foundation through award number CMMI-1652575 and the National Science Foundation Graduate Research Fellowship under Grant No. DGE1255832 is gratefully acknowledged.

Data Availability All relevant data are available from the authors.

Declarations

Conflict of Interest The authors declare that they have no conflict of interest.

References

1. Gibson I, Rosen D, Stucker B, Khorasani M (2021) Additive manufacturing technologies, 3rd edn. Springer. https://doi.org/10.1007/978-3-030-56127-7

2. Seifi M, Gorelik M, Waller J et al (2017) Progress towards metal additive manufacturing standardization to support qualification and certification. JOM 69:439–455. https://doi.org/10.1007/s11837-017-2265-2
3. Nguyen HD, Pramanik A, Basak AK et al (2022) A critical review on additive manufacturing of Ti-6Al-4V alloy: Microstructure and mechanical properties. J Market Res 18:4641–4661. https://doi.org/10.1016/j.jmrt.2022.04.055
4. Gong H, Rafi K, Gu H et al (2014) Analysis of defect generation in Ti-6Al-4V parts made using powder bed fusion additive manufacturing processes. Addit Manuf 1:87–98. https://doi.org/10.1016/j.addma.2014.08.002
5. Kasperovich G, Haubrich J, Gussone J, Requena G (2016) Correlation between porosity and processing parameters in TiAl6V4 produced by selective laser melting. Mater Des 105:160–170. https://doi.org/10.1016/j.matdes.2016.05.070
6. Furton ET, Wilson-Heid AE, Beese AM (2021) Effect of stress triaxiality and penny-shaped pores on tensile properties of laser powder bed fusion Ti-6Al-4V. Addit Manuf 48:102414. https://doi.org/10.1016/j.addma.2021.102414
7. Wilson-Heid AE, Novak TC, Beese AM (2019) Characterization of the effects of internal pores on tensile properties of additively manufactured austenitic stainless steel 316L. Exp Mech 59:793–804. https://doi.org/10.1007/s11340-018-00465-0
8. Wilson-Heid AE, Furton ET, Beese AM (2021) Contrasting the role of pores on the stress state dependent fracture behavior of additively manufactured low and high ductility metals. Materials 14:1–15. https://doi.org/10.3390/ma14133657
9. Chen S, Osovski S (2020) Damage evolution around an embedded pore in quasi-static shear dominant compression and tension specimens. Mech Mater 148:103513. https://doi.org/10.1016/j.mechmat.2020.103513
10. Fadida R, Shirizly A, Rittel D (2020) Static and dynamic shear-compression response of additively manufactured Ti6Al4V specimens with embedded voids. Mech Mater 147:103413. https://doi.org/10.1016/j.mechmat.2020.103413
11. Meng LX, Ben DD, Yang HJ et al (2021) Effects of embedded spherical pore on the tensile properties of a selective laser melted Ti6Al4V alloy. Mater Sci Eng, A 815:141254. https://doi.org/10.1016/j.msea.2021.141254
12. Chobin M (1990) A consideration on stable growth of a ductile crack in a center cracked plate of 70/30 brass. Eng Fract Mech 37:263–273. https://doi.org/10.1016/0013-7944(90)90039-J
13. Rice JR (1964) A path independent integral and the approximate analysis of strain concentration by notches and cracks. Journal of Applied Mechanics, Transactions ASME 35:379–388. https://doi.org/10.1115/1.3601206
14. Rice JR, Drugan WJ, Sham TL (1980) Elastic-plastic analysis of growing cracks. ASTM Special Technical Publication 189–221. https://doi.org/10.1520/stp36972s
15. Lemaitre J, Dufailly J (1987) Damage measurements. Eng Fract Mech 28:643–661. https://doi.org/10.1016/0013-7944(87)90059-2
16. Sancho A, Cox MJ, Cartwright T et al (2016) Experimental techniques for ductile damage characterisation. Procedia Struct Integr 2:966–973. https://doi.org/10.1016/j.prostr.2016.06.124
17. Sheridan L, Gockel JE, Scott-Emuakpor OE (2020) Rapid initiation and growth life characterization of additively manufactured alloy 718 through compliance monitoring. Extreme Mech Lett 40:100856. https://doi.org/10.1016/j.eml.2020.100856
18. Song Y, Magmanlac DJ, Tagarielli VL (2022) A new stiffness-sensing test to measure damage evolution in solids. Sci Rep 12:1–14. https://doi.org/10.1038/s41598-021-04452-9
19. Bonora N, Ruggiero A, Gentile D, de Meo S (2011) Practical applicability and limitations of the elastic modulus degradation technique for damage measurements in ductile metals. Strain 47:241–254. https://doi.org/10.1111/j.1475-1305.2009.00678.x
20. Yoshida F, Uemori T, Fujiwara K (2002) Elastic-plastic behavior of steel sheets under in-plane cyclic tension-compression at large strain. Int J Plast 18:633–659. https://doi.org/10.1016/S0749-6419(01)00049-3
21. ASTM E8/E8M Standard (2010) ASTM E8/E8M standard test methods for tension testing of metallic materials 1. Annual Book of ASTM Standards 4:1–27. https://doi.org/10.1520/E0008
22. 3D Systems (2018) 15-D92 ProX DMP 320 LaserForm Ti Gr23 (A) Best practices
23. Han F, Tang B, Kou H et al (2016) Cyclic softening behavior of Ti–6Al–4V alloy at macro and micro-scale. Mater Lett 185:115–118. https://doi.org/10.1016/j.matlet.2016.08.119
24. Lems W (1962) The change of Young's modulus of copper and silver after deformation at low temperature and its recovery. Physica 28:445–452. https://doi.org/10.1016/0031-8914(62)90022-8
25. Hayter A (2012) Probability and Statistics for Engineers and Scientists, 4th edn. Books/Cole, Cengage Learning, Boston, MA
26. Garrison WM, Moody NR (1987) Ductile fracture. J Phys Chem Solids 48:1035–1074. https://doi.org/10.1016/0022-3697(87)90118-1
27. Wierzbicki T, Bao Y, Lee YW, Bai Y (2005) Calibration and evaluation of seven fracture models. Int J Mech Sci 47:719–743. https://doi.org/10.1016/j.ijmecsci.2005.03.003
28. He MY, Hutchinson JW (1983) Penny-shaped crack in a round bar of power-law hardening material. ASTM Special Technical Publication 291–305
29. O'Dowd NP, Shih CF (1994) Two parameter fracture mechanics: theory and applications, vol 1207. ASTM-STP, American Society for Testing and Materials, Philadelphia, PA, pp 21–47
30. Narra SP, Rollett AD, Ngo A et al (2023) Process qualification of laser powder bed fusion based on processing-defect structure-fatigue properties in Ti-6Al-4V. J Mater Process Technol 311. https://doi.org/10.1016/j.jmatprotec.2022.117775